

Negligible Contribution from Aerosols to Recent Trends in Earth's Energy Imbalance

Chanyoung Park

chanyoung.park@miami.edu

University of Miami https://orcid.org/0000-0001-8644-1031

Brian Soden

University of Miami

Article

Keywords:

Posted Date: March 26th, 2025

DOI: https://doi.org/10.21203/rs.3.rs-5679586/v1

License: © 1 This work is licensed under a Creative Commons Attribution 4.0 International License.

Read Full License

Additional Declarations: There is **NO** Competing Interest.

1 Main Manuscript for

- 2 Negligible Contribution from Aerosols to Recent Trends in Earth's
- 3 Energy Imbalance

4

5 **Competing Interest Statement:** The authors declare no competing interest.

6

- **7 This file includes:**
- 8 Main Text
- 9 Figures 1 to 5

Abstract

During the 21st century, Earth's energy imbalance (EEI) at the top of the atmosphere has markedly increased, mainly due to an increase in absorbed shortwave (SW) rather than a decrease in outgoing longwave (LW) radiation. While previous studies, based on single-forcing (aerosol-only) experiments, linked reductions in anthropogenic aerosols to this positive SW trend, we find that both aerosol-radiation interactions and aerosol-cloud interactions have had a negligible impact on recent increases in the EEI. We estimate recent trends in effective radiative forcing due to aerosols using observations and reanalysis data. While aerosol concentrations have declined in the Northern Hemisphere (NH), wildfires and volcanic activity in the Southern Hemisphere (SH) have resulted in larger aerosol loading. This contrast effectively cancels out the total aerosol forcing, resulting in a negligible global impact on the EEI trend. Our findings also suggest that model-driven estimates may be overestimated, as they overlook the compensating effects of SH aerosol emissions that balance out NH reductions.

Main Text

1. Introduction

The Earth's energy imbalance (EEI) at the top-of-atmosphere (TOA) is a crucial metric for understanding the state of the climate system and an important indicator of climate change (Hansen et al., 2005; Trenberth et al., 2014; Hansen et al., 2017; von Schuckmann et al., 2020). It represents the net difference between the amount of solar energy absorbed by the Earth and the energy radiated back into space, encompassing both incoming shortwave (SW) and outgoing longwave (LW) radiation. Over the past few decades, observations have revealed an increasing trend in EEI, raising concerns about its potential implications for global climate change (e.g., von Schuckmann et al., 2016; Loeb et al., 2018a). Understanding the factors contributing to this trend is essential for accurately predicting future climate scenarios and for formulating effective mitigation strategies.

Recent studies have highlighted a persistent positive trend in EEI over the past two decades, driven primarily by anthropogenic forcing (Kramer et al., 2021; Raghuraman et al., 2021, 2023; Hodnebrog et al., 2024). EEI can be understood as the sum of effective radiative forcing (ERF), which includes rapid adjustments to both natural and anthropogenic forcings, and the radiative

response to these forcings. The latter is influenced by global mean surface temperature changes and the associated climate feedbacks (e.g. Forster et al., 2021; Kramer et al. 2021; Raghuraman et al., 2021).

One of the key factors considered in the context of EEI is the role of aerosols. Aerosols, which include both natural and anthropogenic particles suspended in the atmosphere, interact complexly with both radiation and clouds. These interactions are typically characterized by effective radiative forcing due to aerosol-radiation interactions (ARI) and aerosol-cloud interactions (ACI). ARI, also referred to as aerosol direct effects, involves the direct effects of aerosols on radiation, such as scattering and absorption of sunlight (e.g., Yu et al., 2006). ACI, also known as aerosol indirect effects, refers to the modification of cloud properties by aerosols, influencing cloud reflectivity and longevity (e.g., Twomey, 1977; Albrecht, 1989; Pincus and Baker, 1994).

Analysis using single-forcing (aerosol-only) experiments indicates that effective radiative forcing due to aerosols exhibit positive trends from 2001-2020, driven largely by decays in global aerosol emission in Coupled Model Intercomparison Project Phase 6 (CMIP6) historical and SSP2-4.5 scenarios (Raghuraman et al., 2023). The reduction in aerosol emissions over the Northern Hemisphere (NH) has been identified as a key factor driving the positive trend in EEI, with aerosols' effective radiative forcing accounting for approximately half of the SWTOA trend (Hodnebrog et al., 2024). However, these estimates are model dependent and often lack observational constraints for effective radiative forcing from aerosols, making it challenging to fully assess their impacts on the observed EEI.

To address this gap, our study employs satellite observations and reanalysis data to estimate trends of effective radiative forcing due to aerosols. While previous research has predominantly emphasized the reduction of aerosol emissions in the NH, there has been less attention on the substantial increase in aerosol loading from wildfires and an unexpected volcanic eruption in the Southern Hemisphere (SH) in recent years. These events have introduced large quantities of aerosols into the atmosphere, which provide an interhemispheric contrast with the reductions observed in the NH.

Our findings reveal that aerosols' radiative effects from the SH are substantial enough to offset

those from aerosol reductions in the NH, leading to a negligible global trend from aerosol forcing. This challenges the understanding that declining aerosols in the NH would lead to the positive trend in EEI, suggesting instead that the global impact of aerosols on the EEI trend is minimal although aerosols have influenced regional variations in the EEI. By providing an observationally-based perspective, our research addresses the need for a more accurate understanding of the drivers behind the observed EEI trend. It suggests the importance of factors beyond aerosols, such as natural variability and cloud feedback, in shaping the EEI trend.

83

84

85

86

87

88

89

90

91

92

93

94

95

96

97

98

99

100

101

102

75

76

77

78

79

80

81

82

2. Results

2.1 Observational radiative fluxes

Fig. 1a illustrates the globally averaged monthly anomalies in net TOA radiation (RTOA), SWTOA, and LWTOA, derived from the Clouds and the Earth's Radiant Energy System (CERES) Energy Balanced and Filled (EBAF) Ed. 4.2 satellite observational product (Loeb et al., 2018b). This dataset is known to align well with in-situ observational estimates of energy uptake by Earth's climate system (Loeb et al., 2021a). The linear trend of RTOA reveals a positive slope of 0.51 ± 0.16 W m⁻² decade⁻¹ from 2003 to 2023, indicating a growing disparity between incoming solar and outgoing terrestrial radiation. Specifically, the RTOA trend for the period 2003–2014 is 0.3 ± 0.36 W m⁻² decade⁻¹, while the trend for the more recent period of 2015–2023 is substantially higher at $0.83 \pm 0.53~W~m^{-2}~decade^{-1}$. This trend is driven by the radiative imbalance between the SWTOA and LWTOA components. The strong correlation between RTOA and SWTOA (r = 0.74, p < 0.001), compared to the weaker correlation with LWTOA (r = 0.28, p < 0.001), suggests that the increasing trend in RTOA is primarily driven by a strong positive trend in SWTOA (0.85 \pm 0.14 W m⁻² decade⁻¹), indicating an enhanced absorption of solar radiation by the Earth system. In contrast, the LWTOA exhibits a relatively smaller negative trend of -0.33 ± 0.12 W m⁻² decade⁻¹, which corresponds to an increase in the outgoing longwave radiation that partially offsets the SW-driven warming effect but to a lesser extent. The dominance of the SWTOA in this imbalance is leading to a net positive radiative forcing at the top of the atmosphere, contributing to the ongoing global warming trend.

103104

105

106

107

To identify the specific components of SWTOA that contribute to the strong positive trend, observation-based radiative kernels from Kramer et al. (2019, 2021) were employed. The contributions of the RTOA and LWTOA components are also presented in Supplementary Fig.

1. The SWTOA can be decomposed into contributions from clouds, surface albedo, water vapor, aerosol-radiation interactions, and "others" (Fig. 1b). The "others" category includes contributions from solar irradiance and trace gases (Loeb et al., 2021a). In terms of the global mean, clouds account for 67% (0.57 \pm 0.15 W m⁻² decade⁻¹) of the total positive trend in SWTOA (0.85 \pm 0.14 W m⁻² decade⁻¹), surface albedo explains 25% (0.21 \pm 0.04 W m⁻² decade⁻¹), water vapor contributes 7% (0.06 \pm 0.01 W m⁻² decade⁻¹), aerosol-radiation interactions contribute 3% (0.03 \pm 0.02 W m⁻² decade⁻¹), and the remaining -2% (-0.02 \pm 0.02 W m⁻² decade⁻¹) is attributed to "others". Any changes in SWTOA radiation due to aerosol-cloud interactions are implicitly included in the cloud contribution. These results align with the findings of Loeb et al. (2021a), who used the observation-based partial radiative perturbation (PRP) method to decompose SWTOA radiation from September 2002 to March 2020. They also identified strong contributions from clouds and surface albedo to the positive SWTOA trend, while the contribution of aerosol direct effects (denoted as AER in that paper) was negligible (0.01 \pm 0.04 W m⁻² decade⁻¹). Therefore, in the remainder of this paper, we will focus more specifically on the portion of the SWTOA cloud contribution attributable to aerosol-cloud interactions.

2.2 Recent aerosol concentration trends

In this section, we examine the long-term trends and vertical anomalies in aerosol concentrations, focusing on two metrics: satellite observations of the aerosol index (AI), derived from Moderate Resolution Imaging Spectroradiometer (MODIS; Platnick et al., 2015), and observationally-constrained reanalysis of sulfate aerosol mass concentration (SO₄) at 925 hPa, derived from the Modern-Era Retrospective Analysis for Research and Applications version 2 (MERRA-2; Randles et al., 2017; Gelaro et al., 2017). The spatial distribution of trends in the natural logarithm of AI and SO₄ (Fig. 2a,b) reveals noticeable regional heterogeneity, with contrasting behaviors observed between the Northern and Southern Hemispheres.

In the NH, both AI and SO₄ trends show a marked decrease, particularly over East Asia and North America. This decline is largely attributed to the implementation of stringent air quality regulations aimed at reducing anthropogenic emissions, especially sulfur dioxide (SO₂), a key precursor to sulfate aerosols. The reduction in SO₄ is especially important given its role in influencing cloud formation and scattering solar radiation. The consistent decrease in AI and SO₄ in these regions highlights the effectiveness of pollution control measures over the past

few decades. This is further supported by their vertical profile data, which show positive aerosol anomalies until around 2010, followed by a sustained decline in SO₄ concentrations in both East Asia and North America (Fig. 2c,d).

144

145

146

147

148

149

150

151

152

153

154

155

156

157

158

159

160

161

162

163

164

165

141

142

143

In contrast, the SH presents a different feature, with increasing trends observed in AI and SO₄, particularly over the Southern Ocean and the Southeastern Pacific—regions typically considered relatively pristine with respect to anthropogenic aerosols. These increases have been less anticipated and have not been the focus of as much scientific attention as the NH aerosol reductions. While natural sources such as oceanic emissions of dimethyl sulfide (DMS) contribute to aerosol levels in the SH, recent trends appear to be influenced by episodic extreme events. This recent surge in SH aerosol emission is particularly evident in the vertical profiles of sulfate concentration anomalies. The Southeastern Pacific (Fig. 2e), in particular, shows noticeable peaks in sulfate concentrations in recent years, which correlates with the timing of multiple wildfires in the SH such as the Australian wildfire in 2020 and the Hunga Tonga-Hunga Ha'apai volcanic eruption in 2022 (Supplementary Fig. 2). The impact of these events is further amplified by the climatological westerly winds over the Southern Ocean, which facilitate the transport of aerosols emitted in the Pacific towards the Southeastern Pacific region (Fasullo et al., 2023). This atmospheric circulation pattern enhances the aerosol burden in the Southeastern Pacific, leading to more pronounced anomalies in this area. The increase in the frequency and intensity of such extreme aerosol emission events has resulted in sharp, episodic spikes in aerosol concentrations (Fig. 2e). The vertical profiles emphasize the role of wildfires and the unexpected volcanic eruption, coupled with the climatological westerlies, in driving recent aerosol concentration increases in the SH. This also suggests that the SH could play an increasingly important role in global aerosol distribution, particularly as climate change potentially increases the frequency and severity of such extreme wildfire events (Walker et al., 2019; Jones et al., 2022).

166167

168

169

170

171

172

173

2.3 Observational SW ACI estimates

Now, we estimate the SW ACI using an observationally constrained approach, following the method outlined in Park et al. (2024). This approach shows good agreement of ACI from preindustrial to the present-day with the findings of Bellouin et al. (2020), which employed a process-oriented approach to constrain ACI using multiple lines of evidence from various studies.

It is important to note that our satellite observational data has limited coverage over polar regions and faces challenges in reliably retrieving aerosol-cloud interactions over land (Jia et al., 2019; Gryspeerdt et al., 2022; Jia and Quaas, 2023). Therefore, we focus on the oceanic region between 60°S and 60°N as our main domain of analysis to ensure the reliability of our findings. Furthermore, given that clouds contribute most to the positive SWTOA trend within our study domain, this focus is well-justified (Supplementary Fig. 3).

The SW ACI is estimated using the following equation:

SW ACI
$$\approx \sum_{k=1}^{10} \left(\frac{\partial \text{SWCRE_lcld}}{\partial \ln(N_{\text{d}})} \times \frac{\partial \ln(N_{\text{d}})}{\partial \ln(X)} \right)_k W_k \times \delta \ln(X),$$
 (1)

where SWCRE_lcld represents the cloud radiative effect from non-obscured (non-overlapped) low-level clouds, X represents aerosol concentration proxies either AI or SO₄. N_d represents cloud droplet number concentration and W_k represents the fraction of liquid water path (LWP) in state k ($W_k = \frac{\text{number in LWP state k}}{\text{total number}}$). We employ LWP binning to specifically separate cloud states, building on the method of Park et al. (2024).

We focus on low-level clouds for aerosol-cloud interactions, as they are the dominant contributors to these interactions and ultimately to ACI (Christensen et al., 2016; Bellouin et al., 2020; Forster et al., 2021). The right-hand side of the equation consists of two main components: first, the susceptibility of the low cloud radiative effect to variations in aerosol concentration, determined through cloud controlling factor analysis while holding other environmental influences constant (Scott et al., 2020; Wall et al., 2022), and explicitly incorporating the aerosol activation rate into cloud droplets $(\partial \ln(N_{\rm d})/\partial \ln(X))$; and second, the corresponding monthly anomalies in aerosol concentration relative to the mean for the given time period. Further details regarding this approach and the equation can be found in Park et al. (2024).

Fig. 3a and b shows the susceptibility of both the AI and SO₄, indicating that increases in aerosol concentrations correlate with a negative cloud radiative adjustment, particularly in

regions dominated by low clouds, such as the mid-latitudes in the NH and the Southeastern Pacific. The strong negative susceptibility in this region highlights its important role in enhancing the overall cooling (warming) effect when aerosol concentrations increase (decrease).

The SW ACI trends for both AI and SO₄ (Fig. 3c,d) further illustrate the regional variability in aerosol-cloud interactions. We observe positive SW ACI trends near East Asia and North America, where major industrial regions are located, while strong negative ACI is evident in the Southeastern Pacific, driven primarily by increased aerosol concentration due to wildfires and the volcanic eruption in the SH. The domain-averaged values for both proxies indicate slight negative trends, with a mean value of -0.012 ± 0.04 W m⁻² decade⁻¹ for AI and -0.0003 ± 0.04 W m⁻² decade⁻¹ for SO₄. This value is sufficiently small and can be considered negligible when compared to the global SW cloud component $(0.57 \pm 0.15$ W m⁻² decade⁻¹). It is important to emphasize that the increase in aerosol emissions in the SH, particularly due to wildfires and volcanic activity, has a substantial influence on SW ACI trends, comparable to the impact of reduced aerosol emissions observed in the NH. This strong impact from the SH highlights the hemispheric asymmetry in aerosol-cloud interactions and emphasizes the influence of increased aerosol concentration in the SH, which offset some of the positive radiative forcing from reducing emissions in the NH.

2.4 Comparison with CMIP6 SW ACI

We next investigate the SW ACI trends over the 2003–2023 period using outputs from five models participating in the Radiative Forcing Model Intercomparison Project (RFMIP; Pincus et al., 2016) single-forcing (aerosol-only) experiments. These experiments capture genuine aerosol-cloud interactions that are unaffected by changes in sea surface temperature. To estimate the models' SW ACI, we use the following simplified equation, which was also employed to validate the observationally constrained ACI in Park et al. (2024):

SW ACI =
$$\delta$$
SWCRE_lcld, (2)

where the low-level SW cloud radiative response (δSWCRE_lcld) is determined using the cloud classification method introduced by Webb et al. (2006) and Soden and Vecchi (2011).

Fig. 4 presents the decadal SW ACI trends especially over oceans for three key domains: near-global ($60^{\circ}\text{S}-60^{\circ}\text{N}$), Northern Hemisphere ($0^{\circ}-60^{\circ}\text{N}$), and Southern Hemisphere ($60^{\circ}\text{S}-0^{\circ}$). On a near-global scale (Fig. 4a), the SW ACI trends in the observational estimates for both AI and SO₄ suggest near-zero trends ($-0.012 \pm 0.04 \text{ W m}^{-2}$ decade⁻¹ for AI and $-0.0003 \pm 0.04 \text{ W}$ m⁻² decade⁻¹ for SO₄), indicating minimal change in aerosol-cloud interactions over the past two decades. In contrast, the multi-model mean (MMM) from five models shows a quite strong positive trend (0.14 W m^{-2} decade⁻¹). When examining each model and its realizations individually, the positive values are notably stronger compared to the observational estimates. To better understand the global trends, it is crucial to assess the contributions from each hemisphere separately.

In the NH (Fig. 4b), the RFMIP models project a strong positive SW ACI trend (0.26 W m⁻² decade⁻¹ for MMM), driven primarily by areas near industrial regions such as East Asia and North America, where anthropogenic aerosol emission reductions have been observed (Supplementary Fig. 4). However, the observational estimates reveal a smaller positive trend $(0.04 \pm 0.09 \text{ W m}^{-2} \text{ decade}^{-1} \text{ for AI and } 0.05 \pm 0.1 \text{ W m}^{-2} \text{ decade}^{-1} \text{ for SO}_4$). This discrepancy suggests that the SSP2-4.5 aerosol emission scenario, which serves as the base scenario for RFMIP experiments post-2014, may overestimate the reduction of aerosol concentrations in the NH compared to its actual values. This result is further supported by Supplementary Fig. 5, which illustrates the monthly anomalies of aerosol concentrations from observations compared to those projected under the historical plus SSP2-4.5 scenario. Over the NH, observed aerosol reduction slopes are -0.014 for AI and -0.043 for SO₄, while the MMM shows steeper declines of -0.144 for AI and -0.217 for SO₄, overestimating aerosol concentration reductions by at least a factor of five (Supplementary Fig. 5c,d).

The SH presents more complex features (Fig. 4c). Observational estimates indicate negative SH SW ACI trends (-0.05 ± 0.09 W m⁻² decade⁻¹ for AI and (-0.03 ± 0.09 W m⁻² decade⁻¹ SO₄), which is attributed to the observed increase in aerosol concentrations from wildfires and volcanic activity, particularly in the Southeastern Pacific, where cloud radiative effects exhibit strong negative susceptibility to aerosols. In contrast, the MMM from the models suggests a positive trend (0.06 W m⁻² decade⁻¹) with a broad positive spatial distribution of the SW ACI trend analyzed in the SH for MMM (Supplementary Fig. 4). These differences between observations and models reflect the absence of aerosol emissions from wildfires or volcanic

activity in the models, which are not incorporated into future projections. Some model realizations even exhibit inconsistent signs of SH SW ACI (Fig. 4c).

These features are strongly supported by the aerosol concentration trends between observation data and models results (Supplementary Fig. 5e,f). Noticeable increases aerosol concentrations are observed following wildfire and the volcanic eruption events, while models predict near-neutral aerosol concentration trends. These discrepancies emphasize the need to account for aerosol sources from wildfires or volcanic eruptions as well as their interactions with clouds when interpreting recent changes in EEI. Moreover, the increasing aerosol concentrations in the SH, compared to the reductions observed in the NH, points to an emerging contrast in global aerosol-cloud interactions.

To assess the robustness of our observational estimates, we apply an alternative observationally constrained SW ACI estimation method introduced by Wall et al. (2022). This approach is similar to equation (1) but does not incorporate activation rate and LWP binning. The results provide additional evidence of the impact of increased aerosol concentrations in the SH, with domain averages of -0.303 \pm 0.21 W m⁻² decade⁻¹ for AI and -0.059 \pm 0.03 W m⁻² decade⁻¹ for SO₄ (Fig. 5). These findings reveal an increase in SW ACI in the NH, contrasted by more pronounced negative SH SW ACI trends of -0.54 W m⁻² decade⁻¹ for AI and -0.16 W m⁻² decade⁻¹ for SO₄, resulting in an overall negative contribution of aerosol-cloud interactions to recent EEI trend. This outcome is even more negative than our near-zero estimation, emphasizing the impact of increased aerosol concentrations in the Southern Hemisphere and suggesting that other factors may contribute to the strongly positive SWTOA trend.

3. Conclusion and Discussion

We have examined how aerosols contribute to the recent trend in Earth's energy imbalance through two mechanisms: aerosol-radiation interactions and aerosol-cloud interactions. Despite the recognized warming effects from reduced aerosol concentrations in the NH, the concurrent increase in aerosol concentrations in the SH appears sufficient to counterbalance the warming effects observed in the NH. As a result, while aerosols have played a role in regional EEI variations, their overall contribution to global EEI trends has been minimal over the past few decades.

We also incorporate results from the RFMIP piClim-histnat experiments, which are specifically designed to account for natural sources of aerosol emissions, such as volcanic eruptions, with a particular emphasis on stratospheric aerosols. When examining aerosol-cloud interactions in these experiments, models estimate a slightly negative trend in NH SW ACI of -0.059 W m⁻² decade⁻¹. In contrast, the contribution in the in the SH is negligible, with a trend of -0.004 W m⁻² decade⁻¹ (Supplementary Fig. 6). Overall, single-forcing experiments (both aerosol-only and natural-forcing-only), which employ fixed SST, fail to adequately represent the observed variations in aerosol concentrations and the influences of aerosol-cloud interactions on EEI, despite the limited number of models involved in these experiments.

While our focus has been on aerosols, it is important to acknowledge that other components, such as natural variability and cloud feedback may play dominant roles in shaping the global EEI. For instance, the shift from a negative to a positive Pacific Decadal Oscillation (PDO) index in 2014 has been linked to changes in SST and cloud cover, which likely contributed to variations in EEI (Thorsen, et al., 2018; Loeb et al., 2018a; Loeb et al., 2021a). Following the shift to a positive phase of the PDO in 2014, there was pronounced SST increase, particularly over the eastern Pacific, which persisted through 2020. This warming was accompanied by a reduction in low cloud cover in the region, which led to increased SW along the eastern Pacific, further amplifying the warming (Loeb et al., 2018a). These changes in cloud cover and SW radiation are key drivers in modulating EEI during periods of positive PDO phases. In addition, Raghuraman et al. (2023) highlighted that the observed increase in EEI is driven by the decreased reflection of SW from SW cloud feedback. Unlike LW radiation, which has a stabilizing feedback, Earth's climate system lacks compensating feedbacks in SW. This lack of SW stabilization leads to continuous heat accumulation, contributing to the increasing trend in EEI observed over time.

Methods

In this study, we restrict our analysis to monthly temporal resolution from January 2003 to December 2023, focusing on the geographical coverage spanning from 60°S to 60°N over the ocean, due to unreliable retrievals of satellite observations over land and polar regions (Jia et al., 2019; Gryspeerdt et al., 2022; Jia and Quaas, 2023). All data fields were interpolated onto a 2.5° × 2.5° grid.

Observation and reanalysis data

We use various datasets from the Clouds and the Earth's Radiant Energy System (CERES) for our analysis. To calculate the global trend in top-of-atmosphere (TOA) radiative fluxes, we utilize the CERES Energy Balanced and Filled (EBAF) Ed. 4.2 satellite observational product (Loeb et al., 2018b). For the estimation of shortwave (SW) effective radiative forcing due to aerosol-cloud interactions (ACI), we rely on the CERES FluxByCldTyp Ed. 4.1 dataset (Sun et al., 2022), which allows us to focus on non-obscured (non-overlapped) low-level clouds (Scott et al., 2020), where aerosol-cloud interactions are most relevant (Christensen et al., 2016; Bellouin et al., 2020; Forster et al., 2021). For SW effective radiative forcing due to aerosol-radiation interactions (ARI), we use the CERES EBAF Ed. 4.2 dataset in combination with the CERES SYN1deg Ed. 4A product (Rutan et al., 2015). However, the latter is only employed to estimate aerosol direct effects under clear-sky conditions, as cloud properties derived from geostationary satellites in the SYN1deg product contain artifacts that limit its accuracy in cloudy-sky conditions.

We employ the Moderate Resolution Imaging Spectroradiometer (MODIS; Platnick et al., 2015) data from both the Aqua and Terra satellites (MOD08_M and MYD08_M, respectively) for the aerosol index (AI), which serves as a proxy for aerosol concentration. By combining datasets from the two satellites, we enhance the robustness of our analysis. The AI is derived from the product of aerosol optical depth (AOD) at 550 nm and the Ångström exponent, the latter of which reflects the wavelength dependence of AOD, providing insights into aerosol size distribution (e.g., a smaller Ångström exponent indicates larger particles). AI has shown a stronger correlation with cloud condensation nuclei (CCN) compared to AOD alone (Stier, 2016; Gryspeerdt et al., 2017; Hasekamp et al., 2019). Nevertheless, AI observations remain affected by near-cloud retrieval artifacts (Christensen et al., 2017).

We also utilize the Modern-Era Retrospective analysis for Research and Applications, Version 2 (MERRA-2) reanalysis (Randles et al., 2017; Gelaro et al., 2017). MERRA-2 integrates observations with global model simulations to provide estimates of atmospheric conditions. For example, the total aerosol optical depth is observationally constrained using MODIS satellite data, and the distribution and vertical profiles of different aerosol species are model-derived. Since AI from MODIS provides aerosol species-integrated, column-integrated quantities and does not account for the vertical profile, it may not accurately capture aerosol-

cloud interactions, which mainly occurs in low-level clouds. For SW ACI, we select 925 hPa instead of surface level as our reference, as conditions at 925hPa better reflect CCN concentrations near the cloud base (Painemal et al., 2017). This data is extracted from the 3-hourly MERRA-2 file "inst3_3d_aer_Nv", which we interpolate to monthly resolution for analysis.

We use cloud droplet number concentration (N_d) provided by Gryspeerdt et al. (2022), which was calculated from MODIS cloud optical depth and effective radius. Data from both the Terra and Aqua satellites is combined. N_d measurements can be subject to biases under specific conditions (Zhang and Platnick, 2011; Zhang et al., 2012; Grosvenor and Wood, 2014). To enhance the accuracy and reliability of our N_d retrievals, we apply a rigorous sampling strategy. This approach selects only single-layer liquid clouds that meet predefined criteria, known as the "Z18 sampling" method in Gryspeerdt et al. (2022). These criteria, introduced by Zhu et al. (2018), demonstrate high correlation to in-situ N_d in regions with high cloud fractions (Gryspeerdt et al., 2022). However, the use of different sampling methods introduced in Gryspeerdt et al. (2022) does not affect our conclusions (not shown). Additionally, it is important to note that this dataset was derived from the variables retrieved by MODIS satellite observations and was not filtered to only include low-level clouds. This may have weakened the connection between surface aerosol sources and N_d (McCoy et al., 2018).

For liquid water path (LWP), we use the MODIS MCD06COSP dataset version 6.2.0 (Pincus et al., 2023) and combine data from both the Aqua and Terra satellites. In accordance with the work by Twomey (1977), LWP is crucial in modulating the strength of aerosol-cloud interactions. Moreover, to accurately estimate the aerosol indirect effects, it is essential to control for variations in LWP (Douglas and L'Ecuyer, 2019, 2020), as the relationship between aerosol-cloud interactions and LWP is nonlinear. Isolating this dependence helps minimize its impact on our results (Gryspeerdt et al., 2019). In our analysis, we achieve this by categorizing LWP observations into ten equal bins, each covering a range of 40 g cm⁻², up to a maximum of 400 g cm⁻². This categorization is based on the finding that over 99% of our observations do not exceed 400 g cm⁻², thus allowing us to maintain LWP within a controlled and effectively constant range across our dataset.

CMIP6 data

Previous studies have used Coupled Model Intercomparison Project Phase 6 (CMIP6) models to estimate aerosol contributions to the recent Earth's energy imbalance (EEI) trend, making it essential to compare our observational estimates of aerosol-cloud interactions with those derived from CMIP6 models. To assess the true aerosol effect on the recent EEI, we use single-forcing (aerosol-only) experiments from the Radiative Forcing Model Intercomparison Project (RFMIP; Pincus et al., 2016), specifically the piClim-histaer experiments. These experiments use prescribed sea surface temperatures (SST), and sea ice conditions based on a climatology of pre-industrial conditions and consist of a historical aerosol emission scenario up to 2014, followed by the SSP2-4.5 aerosol emission scenario. We analyze five models that provided extended experiments through 2023, including their available realizations.

Although the piClim-histnat experiment accounts for the influence of volcanic eruptions, it primarily focuses on stratospheric aerosol concentrations from volcanic activity. Therefore, in this study, we use the piClim-histaer experiment as our reference to assess SW ERFaci estimates, employing the first realization (r1) from five models.

Radiative kernel techniques

Radiative kernels, first introduced by Soden and Held (2006) to analyze radiative feedbacks, quantify the differential response of radiative fluxes to small perturbations in key state variables such as clouds, surface albedo, temperature, and water vapor. This allows us to isolate the true cloud radiative response without interference from cloud masking effects. In this study, radiative kernels are applied to deseasonalized monthly anomalies from 2003 to 2023, calculated as deviations from the mean of that period.

For our observational analysis, we use radiative kernels derived from CloudSat/CALIPSO data (Kramer et al., 2019, 2021). Radiative flux anomalies are sourced from the CERES EBAF Ed. 4.2 product (Loeb et al., 2018b). Temperature and specific humidity anomalies are obtained from the ERA5 reanalysis (Hersbach et al., 2020), while surface temperature data is from GISTEMP v4 (Lenssen et al., 2019). Contributions from "others" factors—including solar irradiance and trace gases—are estimated as residuals from all other components (e.g., clouds, albedo, water vapor, and aerosol direct effects) in the total SWTOA. Since aerosol direct effects are not included in our radiative kernel, we estimate them separately as detailed in the section titled "Estimating SW ARI".

For our model analysis, we use radiative kernels derived from the HadGEM3-GA7.1 model (Smith et al., 2020) for CMIP6 model simulations. The HadGEM3-GA7.1 kernel is representative of the commonly used radiative kernels in the literature for tropospheric and surface adjustments (Smith et al., 2020). Differences introduced by using different kernels are less than 0.1 W m⁻² (Soden et al., 2008; Smith et al., 2018).

Estimating SW ARI

To estimate the aerosol direct effects, it is crucial to consider the influence of cloud presence, including factors like cloud height relative to aerosol layers. These factors influence the radiative effects of aerosols. Aerosols located above clouds reduce cloud reflectivity, leading to a relative warming at the TOA, which has a much larger impact compared to the surface (Chand et al., 2009; Wilcox, 2012; Kinne, 2019). Conversely, when clouds are positioned above aerosols, they can block aerosol interactions with solar radiation. Moreover, clouds can either enhance atmospheric heating from absorbing aerosols or can mask the cooling effect of scattering aerosols (Soden et al. 2004; Matus et al. 2015).

In this study, we classify sky conditions as either cloudy or clear to capture these variations in radiative effects at the TOA. The contribution of each aerosol direct effect is weighted by both the cloud fraction and the clear-sky fraction (Matus et al., 2015). Our analysis primarily uses CERES product, and the estimation of SW ARI is based on the following equation:

SW ARI =
$$\delta$$
(SW DRE_{cld} × CF) + δ (SW DRE_{clr} × (1 – CF)), (1)

where SW DRE_{cld} refers to the SW aerosol direct radiative effects (DRE) under cloudy-sky conditions, SW DRE_{clr} refers to the SW DRE under clear-sky conditions, and CF represents the cloud fraction. The first term on the right-hand side represents the monthly anomalies of the aerosol direct effect under cloudy sky, weighted by cloud fraction, while the second term represents the effect under clear sky, weighted by clear sky fraction.

Estimating aerosol direct effects requires a radiative transfer model to assess the difference between conditions with and without aerosols. The estimate of SW DRE_{cld} relies on MERRA-2 due to the absence of a radiative transfer model for CERES. However, SW DRE_{clr} is estimated

using the method described in Loeb et al. (2021b), which combines calculated fluxes from the CERES SYN1deg Ed. 4A dataset (Rutan et al., 2015) with observed fluxes from the CERES EBAF Ed4.2 (Loeb et al., 2018b). This approach accounts for the masking effect of aerosols on surface albedo variations caused by the presence of aerosols.

Using MERRA-2 reanalysis data for SW DRE_{cld} while relying on CERES for other components may introduce some uncertainty into our SW ARI estimates as cloudy-sky conditions can modulate the radiative forcing of aerosols differently compared to clear-sky conditions. However, given that aerosol-radiation interactions have been shown to exert a relatively negligible influence on the trend in EEI in both this study and previous study (Loeb et al., 2021a), the overall uncertainty introduced by this limitation is not expected to alter our conclusions.

Uncertainty from estimating SW ACI trend

Unlike aerosol concentration trends observed directly, estimating aerosol-cloud interactions introduces additional uncertainties due to the complex calculations involved in the estimation process, as described in Park et al. (2024). Therefore, we account for these uncertainties by combining those arising from susceptibility with those from the observed aerosol concentration trend.

To quantify the uncertainty in the regression coefficients of susceptibility, a 90% confidence interval for susceptibility at each grid box is calculated as follows:

$$\delta = t \sqrt{\Delta x^{\mathrm{T}} \mathbf{C} \Delta x} \sqrt{\frac{N_{\mathrm{nom}}}{N_{\mathrm{eff}}}}, \tag{2}$$

where t is the critical value of the Student's t-test at the 95% significance level with $N_{\rm eff} - 7$ degrees of freedom (Storch and Zwiers, 1999), C represents the variance–covariance matrix of regression coefficients, $N_{\rm nom}/N_{\rm eff}$ is the ratio of the nominal to effective number of monthly anomalies of SWCRE_lcld, and Δx is the regression coefficient for $\partial \ln(N_{\rm d})/\partial \ln(X)$, where X represents either AI or SO₄. C is formulated as $C = \hat{\sigma}^2(Z^TZ)^{-1}$, where Z is the data matrix with columns composed of detrended monthly anomalies, specifically in terms of $\ln(N_{\rm d})$. The

term $\hat{\sigma}^2$ denotes the mean of squared residuals of the regression model and we estimate $N_{\text{nom}}/N_{\text{eff}}$ as (1 + r)/(1 - r), where r is the lag one autocorrelation of monthly anomalies of SWCRE_lcld.

503

504

506

507

508

509

510

511

512

513

Uncertainty for spatially averaged regression coefficients is calculated as

$$\Delta_{\text{susceptibility}} = \sqrt{\frac{\sum_{k=1}^{N_{\text{nom}}^*} (\delta_k w_k)^2}{\left(\sum_{k=1}^{N_{\text{nom}}^*} w_k\right)^2}} \sqrt{\frac{N_{\text{nom}}^*}{N_{\text{eff}}^*}} , \qquad (3)$$

where δ_k represents the uncertainty in the kth grid box, while w_k corresponds to the cosine of the latitude. N_{nom}^* represents the nominal number of spatial degrees of freedom, and N_{eff}^* refers to the effective number of spatial degrees of freedom. The ratio $N_{\text{nom}}^*/N_{\text{eff}}^*$ is calculated using empirical orthogonal function (EOF) analysis on SWCRE_lcld anomalies across all ocean grid between 60°S and 60°N, following equation 5 from Bretherton et al. (1999). Prior to conducting the EOF analysis, the monthly anomalies of SWCRE_lcld for each grid are multiplied by $\sqrt{w_k}$ to reduce the influence of grid geometry (North et al. 1982). The resulting $\Delta_{\text{susceptibility}}$ represents the half-width of the 90% CI for SW ACI, specifically reflecting the uncertainty associated with regression coefficients of susceptibility.

515

516

517

518

514

To estimate the uncertainty derived from the aerosol concentration trend of ln(X), we apply the method described in Santer et al. (2000), which accounts for autocorrelation in the data, Δ_{trend} . Thus, the overall 90% CI is expressed as follows:

519

SW ACI
$$\pm \sqrt{\Delta_{\text{susceptibility}}^2 + \Delta_{\text{trend}}^2}$$
. (4)

521 522

523

524

525

526

527

528

Data Availability

The CERES data used in this study were obtained from NASA's CERES ordering tool (https://ceres.larc.nasa.gov/data/). MODIS data were sourced from NASA's Level-1 and Atmosphere Archive and Distribution System (https://ladsweb.modaps.eosdis.nasa.gov/archive/allData/61/), while MODIS N_d data are accessible through Environmental Data **Analysis** the Centre for (https://doi.org/10.5285/864a46cc65054008857ee5bb772a2a2b, Gryspeerdt et al., 2022). The

- 529 MERRA-2 reanalysis data were downloaded via NASA Goddard Earth Sciences Data and
- Information Services Center (https://doi.org/10.5067/LTVB4GPCOTK2). CMIP6 data
- employed in this research can be found on the Earth System Grid Federation data portal
- 532 (https://esgf-node.llnl.gov/projects/cmip6/).

534

References

- 1. Hansen, J. et al. Efficacy of climate forcings. Journal of Geophysical Research:
- 536 Atmospheres 110, (2005).
- 2. Trenberth, K. E., Fasullo, J. T. & Balmaseda, M. A. Earth's Energy Imbalance. (2014)
- 538 doi:10.1175/JCLI-D-13-00294.1.
- 3. Hansen, J. et al. Young people's burden: requirement of negative CO2 emissions. Earth
- 540 System Dynamics 8, 577–616 (2017).
- 4. von Schuckmann, K. et al. Heat stored in the Earth system: where does the energy go? Earth
- 542 System Science Data 12, 2013–2041 (2020).
- 5. von Schuckmann, K. et al. An imperative to monitor Earth's energy imbalance. Nature Clim
- 544 Change 6, 138–144 (2016).
- 6. Loeb, N. G., Thorsen, T. J., Norris, J. R., Wang, H. & Su, W. Changes in Earth's Energy
- Budget during and after the "Pause" in Global Warming: An Observational Perspective.
- 547 Climate 6, 62 (2018).
- 548 7. Kramer, R. J. et al. Observational Evidence of Increasing Global Radiative Forcing.
- Geophysical Research Letters 48, e2020GL091585 (2021).
- 8. Raghuraman, S. P., Paynter, D. & Ramaswamy, V. Anthropogenic forcing and response
- yield observed positive trend in Earth's energy imbalance. Nat Commun 12, 4577 (2021).
- 9. Raghuraman, S. P., Paynter, D., Menzel, R. & Ramaswamy, V. Forcing, Cloud Feedbacks,
- Cloud Masking, and Internal Variability in the Cloud Radiative Effect Satellite Record.
- Journal of Climate 36, 4151–4167 (2023).
- 10. Hodnebrog, Ø. et al. Recent reductions in aerosol emissions have increased Earth's energy
- imbalance. Commun Earth Environ 5, 1–9 (2024).
- 11. Forster, P. et al. in Climate Change 2021: The Physical Science Basis (eds Masson-

- Delmotte, V. et al.) 923–1054 (Cambridge Univ. Press, 2021).
- 12. Yu, H. et al. A review of measurement-based assessments of the aerosol direct radiative
- effect and forcing. Atmospheric Chemistry and Physics 6, 613–666 (2006).
- 13. Twomey, S. The Influence of Pollution on the Shortwave Albedo of Clouds. Journal of the
- 562 Atmospheric Sciences 34, 1149–1152 (1977).
- 14. Albrecht, B. A. Aerosols, Cloud Microphysics, and Fractional Cloudiness. Science 245,
- 564 1227–1230 (1989).
- 15. Pincus, R. & Baker, M. B. Effect of precipitation on the albedo susceptibility of clouds in
- the marine boundary layer. Nature 372, 250–252 (1994).
- 16. Loeb, N. G. et al. Clouds and the Earth's Radiant Energy System (CERES) Energy
- Balanced and Filled (EBAF) Top-of-Atmosphere (TOA) Edition-4.0 Data Product. (2018)
- doi:10.1175/JCLI-D-17-0208.1.
- 17. Loeb, N. G. et al. Satellite and Ocean Data Reveal Marked Increase in Earth's Heating Rate.
- Geophysical Research Letters 48, e2021GL093047 (2021).
- 18. Kramer, R. J., Matus, A. V., Soden, B. J. & L'Ecuyer, T. S. Observation-Based Radiative
- Kernels From CloudSat/CALIPSO. Journal of Geophysical Research: Atmospheres 124,
- 574 5431–5444 (2019).
- 19. Platnick, S., M. King, P. Hubanks. MODIS Atmosphere L3 Monthly Product. NASA
- 576 MODIS Adaptive Processing System, Goddard Space Flight Center,
- 577 http://dx.doi.org/10.5067/MODIS/MOD08 M3.061;
- 578 <u>http://dx.doi.org/10.5067/MODIS/MYD08_M3.061</u> (2015).
- 579 20. Randles, C. A. et al. The MERRA-2 Aerosol Reanalysis, 1980 Onward. Part I: System
- Description and Data Assimilation Evaluation. Journal of Climate 30, 6823–6850 (2017).
- 21. Gelaro, R. et al. The Modern-Era Retrospective Analysis for Research and Applications,
- Version 2 (MERRA-2). Journal of Climate 30, 5419–5454 (2017).
- 583 22. Fasullo, J. T., Rosenbloom, N. & Buchholz, R. A multiyear tropical Pacific cooling
- response to recent Australian wildfires in CESM2. Science Advances 9, eadg1213 (2023).
- 585 23. Walker, X. J. et al. Increasing wildfires threaten historic carbon sink of boreal forest soils.

- 586 Nature 572, 520–523 (2019).
- 587 24. Jones, M. W. et al. Global and Regional Trends and Drivers of Fire Under Climate Change.
- Reviews of Geophysics 60, e2020RG000726 (2022).
- 25. Park, C., Soden, B. J., Kramer, R. J., L'Ecuyer, T. S. & He, H. Observational Constraints
- Suggest a Smaller Effective Radiative Forcing from Aerosol-Cloud Interactions.
- EGUsphere 1–39 (2024) doi:10.5194/egusphere-2024-2547.
- 592 26. Bellouin, N. et al. Bounding Global Aerosol Radiative Forcing of Climate Change. Reviews
- of Geophysics 58, e2019RG000660 (2020).
- 594 27. Jia, H., Ma, X., Quaas, J., Yin, Y. & Qiu, T. Is positive correlation between cloud droplet
- effective radius and aerosol optical depth over land due to retrieval artifacts or real physical
- processes? Atmospheric Chemistry and Physics 19, 8879–8896 (2019).
- 597 28. Gryspeerdt, E. et al. The impact of sampling strategy on the cloud droplet number
- concentration estimated from satellite data. Atmospheric Measurement Techniques 15,
- 599 3875–3892 (2022).
- 29. Jia, H. & Quaas, J. Nonlinearity of the cloud response postpones climate penalty of
- mitigating air pollution in polluted regions. Nat. Clim. Chang. 13, 943–950 (2023).
- 30. Christensen, M. W., Chen, Y.-C. & Stephens, G. L. Aerosol indirect effect dictated by liquid
- clouds. Journal of Geophysical Research: Atmospheres 121, 14,636-14,650 (2016).
- 31. Scott, R. et al. Observed Sensitivity of Low-Cloud Radiative Effects to Meteorological
- Perturbations over the Global Oceans. Journal of Climate 33, (2020).
- 32. Wall, C. J. et al. Assessing effective radiative forcing from aerosol-cloud interactions over
- the global ocean. Proc. Natl. Acad. Sci. U.S.A. 119, e2210481119 (2022).
- 33. Pincus, R., Forster, P. M. & Stevens, B. The Radiative Forcing Model Intercomparison
- Project (RFMIP): experimental protocol for CMIP6. Geoscientific Model Development 9,
- 610 3447–3460 (2016).
- 34. Webb, M. J. et al. On the contribution of local feedback mechanisms to the range of climate
- sensitivity in two GCM ensembles. Clim Dyn 27, 17–38 (2006).
- 35. Soden, B. J. & Vecchi, G. A. The vertical distribution of cloud feedback in coupled ocean-

- atmosphere models. Geophysical Research Letters 38, (2011).
- 36. Thorsen, T. J., Kato, S., Loeb, N. G. & Rose, F. G. Observation-Based Decomposition of
- Radiative Perturbations and Radiative Kernels. (2018) doi:10.1175/JCLI-D-18-0045.1.
- 37. Sun, M. et al. Clouds and the Earth's Radiant Energy System (CERES) FluxByCldTyp
- Edition 4 Data Product. (2022) doi:10.1175/JTECH-D-21-0029.1.
- 38. Rutan, D. A. et al. CERES Synoptic Product: Methodology and Validation of Surface
- Radiant Flux. (2015) doi:10.1175/JTECH-D-14-00165.1.
- 39. Stier, P. Limitations of passive remote sensing to constrain global cloud condensation nuclei.
- 622 Atmos. Chem. Phys. 16, 6595–6607 (2016).
- 623 40. Gryspeerdt, E. et al. Constraining the instantaneous aerosol influence on cloud albedo.
- Proceedings of the National Academy of Sciences 114, 4899–4904 (2017).
- 625 41. Hasekamp, O. P., Gryspeerdt, E. & Quaas, J. Analysis of polarimetric satellite
- measurements suggests stronger cooling due to aerosol-cloud interactions. Nat Commun
- 627 10, 5405 (2019).
- 42. Painemal, D. et al. Aerosol and cloud microphysics covariability in the northeast Pacific
- boundary layer estimated with ship-based and satellite remote sensing observations.
- Journal of Geophysical Research: Atmospheres 122, 2403–2418 (2017).
- 43. Zhang, Z. & Platnick, S. An assessment of differences between cloud effective particle
- radius retrievals for marine water clouds from three MODIS spectral bands. Journal of
- Geophysical Research: Atmospheres 116, (2011).
- 44. Zhang, Z. et al. Effects of cloud horizontal inhomogeneity and drizzle on remote sensing
- of cloud droplet effective radius: Case studies based on large-eddy simulations. Journal of
- Geophysical Research: Atmospheres 117, (2012).
- 45. Grosvenor, D. P. & Wood, R. The effect of solar zenith angle on MODIS cloud optical and
- microphysical retrievals within marine liquid water clouds. Atmospheric Chemistry and
- Physics 14, 7291–7321 (2014).
- 46. Zhu, Y., Rosenfeld, D. & Li, Z. Under What Conditions Can We Trust Retrieved Cloud
- Drop Concentrations in Broken Marine Stratocumulus? Journal of Geophysical Research:
- 642 Atmospheres 123, 8754–8767 (2018).

- 47. McCoy, D. T. et al. Predicting decadal trends in cloud droplet number concentration using
- reanalysis and satellite data. Atmospheric Chemistry and Physics 18, 2035–2047 (2018).
- 48. Pincus, R. et al. Updated observations of clouds by MODIS for global model assessment.
- Earth System Science Data 15, 2483–2497 (2023).
- 49. Douglas, A. & L'Ecuyer, T. Quantifying variations in shortwave aerosol-cloud-radiation
- interactions using local meteorology and cloud state constraints. Atmospheric Chemistry
- and Physics 19, 6251–6268 (2019).
- 50. Douglas, A. & L'Ecuyer, T. Quantifying cloud adjustments and the radiative forcing due to
- aerosol-cloud interactions in satellite observations of warm marine clouds. Atmos. Chem.
- Phys. 20, 6225–6241 (2020).
- 653 51. Gryspeerdt, E. et al. Constraining the aerosol influence on cloud liquid water path.
- Atmospheric Chemistry and Physics 19, 5331–5347 (2019).
- 52. Soden, B. J. & Held, I. M. An Assessment of Climate Feedbacks in Coupled Ocean-
- 656 Atmosphere Models. (2006) doi:10.1175/JCLI3799.1.
- 53. Hersbach, H. et al. The ERA5 global reanalysis. Quarterly Journal of the Royal
- Meteorological Society 146, 1999–2049 (2020).
- 54. Lenssen, N. J. L. et al. Improvements in the GISTEMP Uncertainty Model. Journal of
- Geophysical Research: Atmospheres 124, 6307–6326 (2019).
- 55. Smith, C. J., Kramer, R. J. & Sima, A. The HadGEM3-GA7.1 radiative kernel: the
- importance of a well-resolved stratosphere. Earth System Science Data 12, 2157–2168
- 663 (2020).
- 56. Soden, B. J. et al. Quantifying Climate Feedbacks Using Radiative Kernels. Journal of
- 665 Climate 21, 3504–3520 (2008).
- 57. Smith, C. J. et al. Understanding Rapid Adjustments to Diverse Forcing Agents.
- Geophysical Research Letters 45, 12,023-12,031 (2018).
- 58. Chand, D., Wood, R., Anderson, T. L., Satheesh, S. K. & Charlson, R. J. Satellite-derived
- direct radiative effect of aerosols dependent on cloud cover. Nature Geosci 2, 181–184
- 670 (2009).

- 59. Wilcox, E. M. Direct and semi-direct radiative forcing of smoke aerosols over clouds.
- Atmospheric Chemistry and Physics 12, 139–149 (2012).
- 60. Kinne, S. Aerosol radiative effects with MACv2. Atmospheric Chemistry and Physics 19,
- 674 10919–10959 (2019).
- 61. Soden, B. J., Broccoli, A. J. & Hemler, R. S. On the Use of Cloud Forcing to Estimate
- 676 Cloud Feedback. (2004).
- 62. Matus, A. V., L'Ecuyer, T. S., Kay, J. E., Hannay, C. & Lamarque, J.-F. The Role of Clouds
- in Modulating Global Aerosol Direct Radiative Effects in Spaceborne Active Observations
- and the Community Earth System Model. (2015) doi:10.1175/JCLI-D-14-00426.1.
- 680 63. Loeb, N. G., Su, W., Bellouin, N. & Ming, Y. Changes in Clear-Sky Shortwave Aerosol
- Direct Radiative Effects Since 2002. Journal of Geophysical Research: Atmospheres 126,
- e2020JD034090 (2021).
- 64. Storch, H. von & Zwiers, F. W. Statistical Analysis in Climate Research. (Cambridge
- University Press, Cambridge, 1999). doi:10.1017/CBO9780511612336.
- 65. Bretherton, C. S., Widmann, M., Dymnikov, V. P., Wallace, J. M. & Bladé, I. The Effective
- Number of Spatial Degrees of Freedom of a Time-Varying Field. Journal of Climate 12,
- 687 1990–2009 (1999).
- 688 66. North, G. R., Bell, T. L., Cahalan, R. F. & Moeng, F. J. Sampling Errors in the Estimation
- of Empirical Orthogonal Functions. Monthly Weather Review 110, 699–706 (1982).
- 690 67. Santer, B. D. et al. Statistical significance of trends and trend differences in layer-average
- atmospheric temperature time series. Journal of Geophysical Research: Atmospheres 105,
- 692 7337–7356 (2000).

694

695

696

Figures

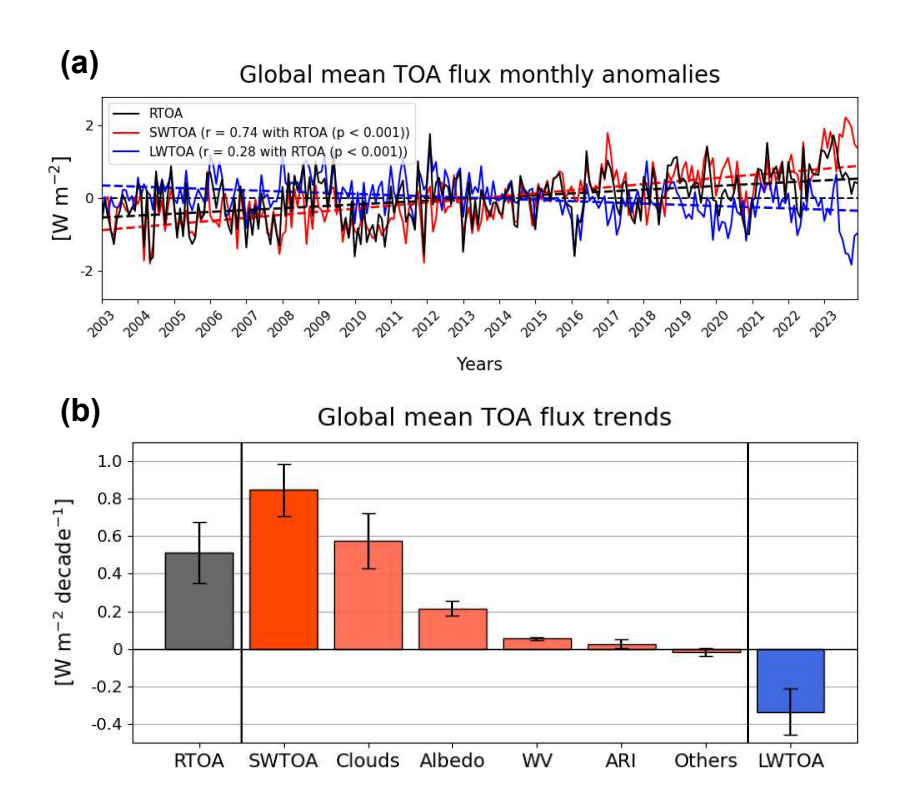


Fig. 1. Global mean top-of-atmosphere (TOA) flux monthly anomalies and trends from 2003 to 2023. (a) Global mean monthly anomalies of net TOA radiation (RTOA; black solid line), along with the shortwave (SWTOA; red solid line) and longwave (LWTOA; blue solid line) components. Dashed lines show the linear trends for each component. Correlation coefficients (*r*) and associated *p*-values (*p*) between RTOA and SWTOA, as well as RTOA and LWTOA, are provided in the upper-left corner. (b) Global mean TOA flux trends in RTOA, SWTOA, with contributions from changes in clouds, albedo, water vapor (WV), aerosol-radiation interactions (ARI), and combined effects of trace gases, and solar irradiance (labeled as "Others"), as well as trend in LWTOA calculated by observationally-based radiative kernel method (Kramer et al., 2019, 2021). Error bars represent the 5–95% confidence intervals, calculated following the methodology of Santer et al. (2000). Positive anomalies indicate Earth absorbing more energy, while negative anomalies represent energy loss.

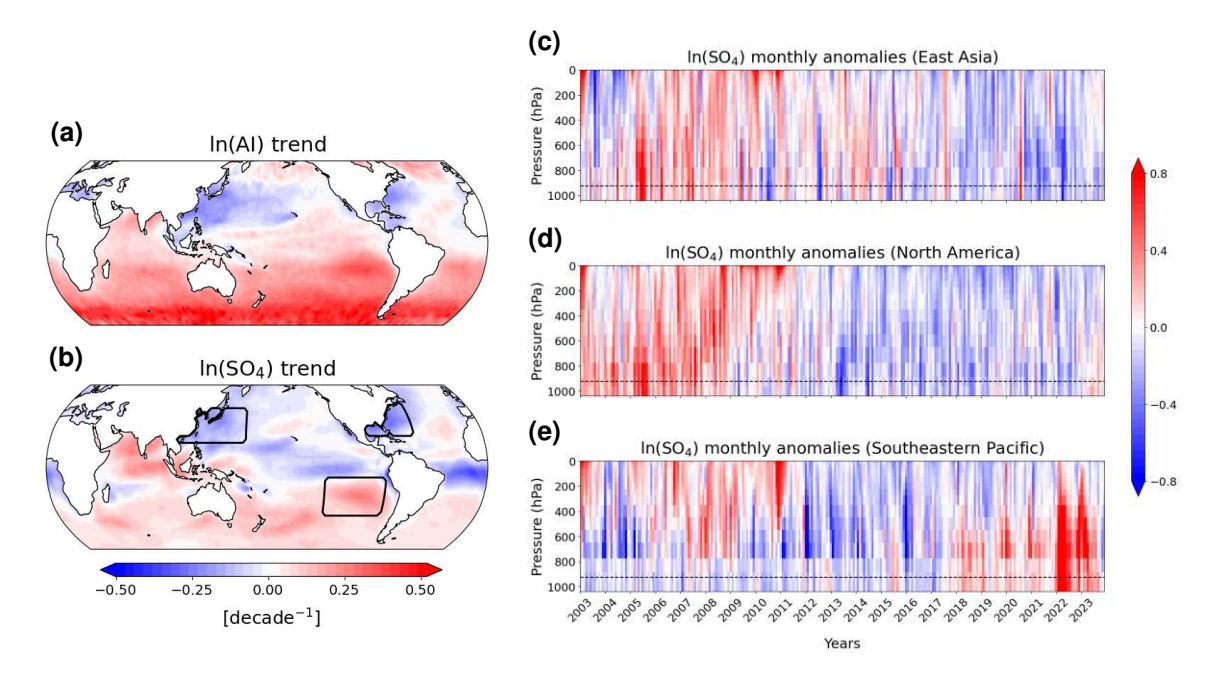


Fig. 2. Decadal trends and monthly anomalies in the natural logarithm of aerosol proxies. (a) Spatial maps of trends in the natural logarithm of the aerosol index (AI) and (b) sulfate aerosol mass concentration (SO₄) at 925 hPa for the period 2003–2023. (c–e) Vertical distributions of ln(SO₄) monthly anomalies over the boxed regions in (b): (c) East Asia, (d) North America, and (e) the Southeastern Pacific. The dashed line in each panel represents the 925 hPa pressure level.

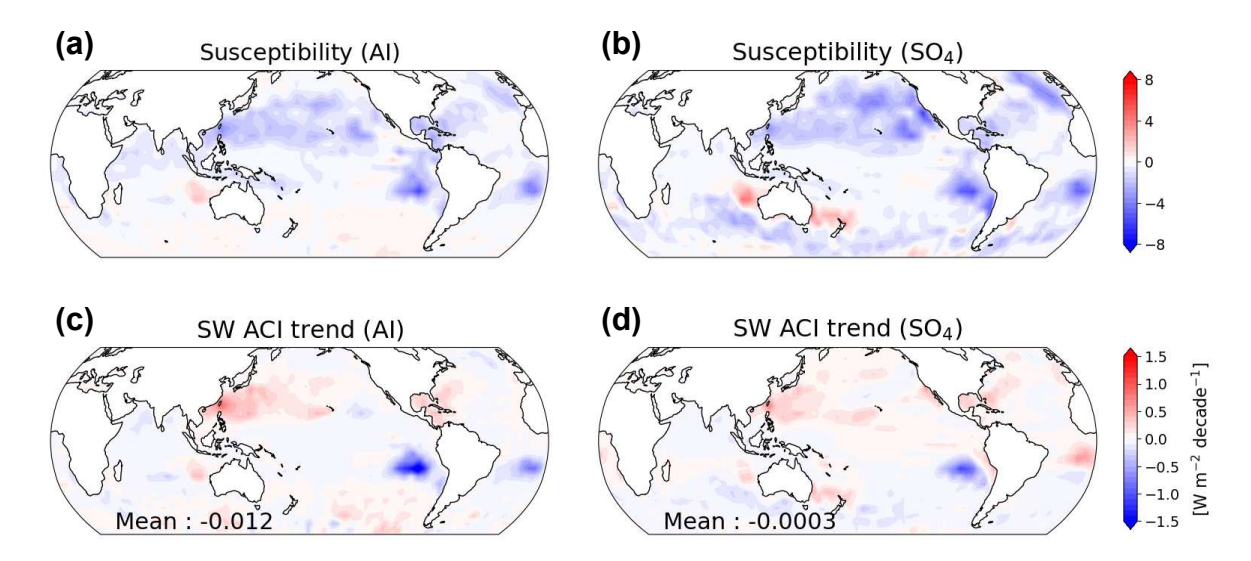


Fig. 3. Spatial distributions of non-obscured low cloud susceptibility to variations in aerosol concentrations and decadal trends in shortwave (SW) effective radiative forcing from aerosol-cloud interactions (ACI), differentiated by aerosol proxies. (a) Susceptibility for the AI. (b) Same as (a), but for SO₄. (c) Observationally constrained SW ACI trend for AI from 2003 to 2023. (d) Same as (c), but for SO₄. The domain-averaged (60°S–60°N, ocean) SW ACI values are shown in the lower-left corners of each panel.

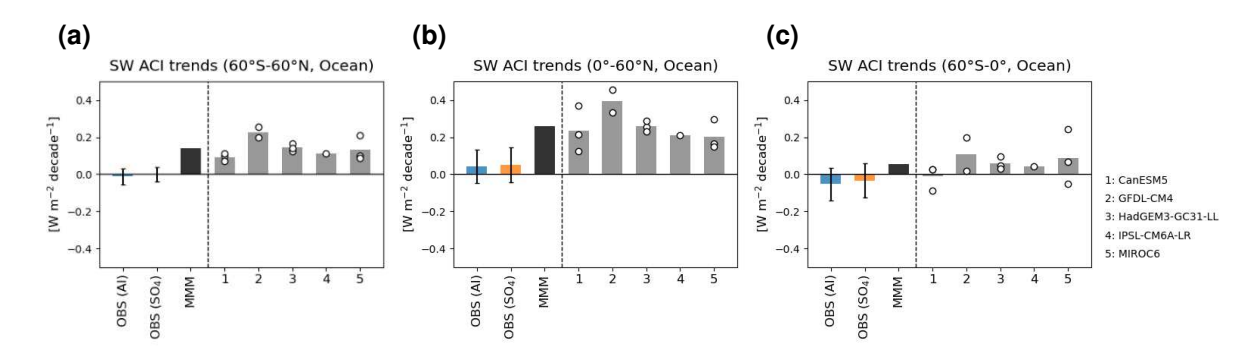


Fig. 4. Decadal trends in SW ACI over oceans across three different domains: (a) near-global (60°S–60°N), (b) Northern Hemisphere (NH; 0°–60°N), and (c) Southern Hemisphere (SH; 60°S–0°). Observationally constrained SW ACI estimates are derived from two aerosol proxies: aerosol index (AI, blue) and sulfate aerosol mass concentrations (SO₄, orange). Uncertainties are calculated by combining the methods from Park et al. (2024) and Santer et al. (2000) (Methods). The multi-model mean (MMM, black) is derived from five models in the Radiative Forcing Model Intercomparison Project (RFMIP; Pincus et al., 2016) single-forcing (aerosolonly) experiments. Individual model realizations are depicted as hollow circles, with grey bars representing the mean of these realizations.

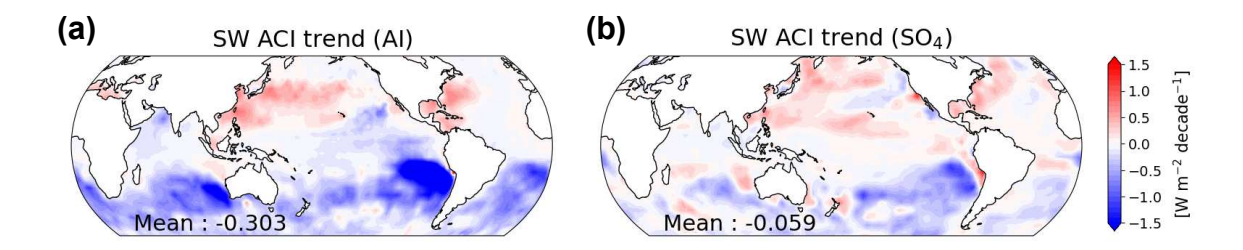


Fig. 5. Spatial distributions of observationally constrained SW ACI trends from 2003 to 2023, using an alternative method based on Wall et al. (2022). (a) SW ACI trend for AI. (b) Same as (a), but for SO₄. The domain-averaged (60°S–60°N, ocean) SW ACI values are shown in the lower-left corners of each panel.

Supplementary Files

This is a list of supplementary files associated with this preprint. Click to download.

• NCCSupplementaryinitialsubmission.docx